Experimental Mechanics (2019) 59:111–120
https://doi.org/10.1007/s11340-018-00447-2

Residual Stresses in Cu/Ni Multilayer Thin Films Measured Using the Sin^{2}ψ Method

I.G. McDonald [1] · W.M. Moehlenkamp [2] · D. Arola [1,2] · J. Wang [1]

Received: 4 June 2018 / Accepted: 22 October 2018 / Published online: 8 November 2018

Abstract

Residual stresses in multilayer thin films are of substantial importance to the service life of advanced engineering systems. In this investigation, the residual stresses in magnetron sputtered Cu/Ni multilayer thin films were characterized using x-ray diffraction (XRD) and the sin^{2}ψ method. The influence of layer thickness on residual stress was explored for films with alternating Ni and Cu layers with equal layer thicknesses ranging from 10 nm to 100 nm. To address peak broadening and overlapping, the Gaussian Mixture Model (GMM) and Expectation Maximization (EM) algorithm were employed, and the peak position was determined using the Center of Gravity (CoG) method. Results showed tensile residual stress in both the Cu and Ni layers and a prominent layer thickness dependence. The stress in the Ni layers increased from roughly 880 MPa to 1550 MPa with decreasing layer thickness from 100 nm to 10 nm. In the Cu layers, the stress remained relatively constant at ~250 MPa and then substantially decreased for the 10 nm thickness. The findings confirm that the XRD-based approach can be applied for residual stress measurement in nanoscale multilayer thin films, provided that peak broadening and overlapping issues are addressed. Furthermore, the residual stress in metal multilayers is strongly dependent on layer thickness.

Keywords Residual stress · Multilayer thin-films · Nanolaminates · sin^{2}ψ method · X-ray diffraction

Introduction

In the fields of electronics, clean energy technology, and micro electromechanical systems (MEMs), materials are being created to meet increasing mechanical, optical and electrical performance requirements. Multilayer thin film systems show tremendous promise in this area. These materials have demonstrated substantially larger hardness and strength when compared to their bulk counterparts. In addition, many of their mechanical properties can be controlled by adjusting layer thickness and by post processing treatments [1–5]. Multilayer films also show improved thermal stability [5, 6] and optoelectronic properties [7] with respect to monolithic films. Despite these desirable qualities, residual stresses within the multilayer thin films are a primary concern.

✉ J. Wang
junlan@u.washington.edu

[1] Department of Mechanical Engineering, University of Washington, Seattle, WA, USA

[2] Department of Material Science and Engineering, University of Washington, Seattle, WA, USA

Residual stress often develops during the deposition and growth of thin films [8]. Coalescence of grain boundaries during film growth [8, 9] is a potential source of residual stress. Excessively high residual stress magnitudes may cause delamination, buckling and microcracking [10, 11]. As such, it is important to understand the residual stress state and magnitude, as well as their dependency on processing conditions. For tensile residual stress, the risk of delamination increases with total film thickness [10], which necessitates a lower overall film thickness to avoid delamination. Prior work on Cu/Cr multilayers suggests that the residual stress in multilayer thin films is dependent on layer thickness and increases with decreasing layer thickness down to 50 nm [4]. High tensile residual stresses may result in cracking, a decrease in wear resistance and poor fatigue strength, while compressive stress has been shown to be beneficial [12].

Residual stress in thin films is typically measured using wafer curvature or X-ray diffraction (XRD) techniques. Wafer curvature methods measure the curvature of the film/substrate system and utilize the Stoney formula to compute an average in-plane stress [13, 14]. One advantage of this technique is that it can be used to measure the stress in both amorphous and crystalline films [14, 15]. The drawback, however, is that for a multilayer system the wafer curvature

technique only provides an average stress for the entire multilayer stack. It is possible to measure the change in stress after or during layer formation, to investigate the layer contribution individually. However, these processes often involve cumbersome *in-situ* curvature monitoring techniques or require post-process etching removal of layers [14–16].

For crystalline materials, XRD uses constructive interference of monochromatic X-rays at Bragg angles to measure the interplanar lattice spacing. This acts as an internal strain gauge by which the stress can be calculated. The $\sin^2\psi$ technique can then be incorporated with XRD measurements of the lattice spacing to calculate the residual stress based on the lattice strain and Hooke's law [17]. One distinct advantage of the XRD approach over the wafer curvature technique is that it can distinguish stress in one material composition from the stress in another, provided both compositions are polycrystalline and the substrate does not contribute to the stress state [14, 18].

In the present investigation, the residual stresses in Cu/Ni multilayer thin films were explored. Preliminary testing was performed using two-dimensional (2D) XRD and the XRD^2 method to verify that the films exhibited an equi-biaxial stress state. A common challenge when working with nanometer-scale thin films is the low signal intensity and peak broadening due to small grain size [19], both of which complicate the determination of the residual stress magnitude precisely. When evaluating multilayer and especially multi-material systems, peak broadening can lead to peak overlap, which increases the difficulty to determine the diffracted peak locations. Due to this challenge, a traditional 1D XRD and the $\sin^2\psi$ method was performed to estimate the in-plane residual stress; the Gaussian Mixture Model and Expectation Maximization algorithm were adopted to separate the overlapping peaks from the 1D scans. Then, the center of gravity method was used for determining the diffracted peak positions, which has been recommended for achieving low standard deviation [20].

Experimental Methods

Sample Preparation

Cu/Ni multilayer thin films with individual layer thickness of 100, 50, 25, and 10 nm were deposited at 18 °C on single crystal (100) Si substrates rotating at 20 rpm using an Orion-5-UHV dual DC magnetron sputtering system (AJA International Inc.). The individual Cu and Ni layers were sputtered to achieve equal layer thicknesses using a 100 W DC power with a sputtering rate of 12 nm/min and 5.1 nm/min, respectively. A Ti adhesion layer of approximately 10 nm thickness was deposited onto the Si substrates first using a RF power of 120 W and a rate of 0.5 nm/min. Both the Cu and Ni targets had a purity of 99.99% and the Ti target had a purity of 99.995%. The base pressure for the vacuum chamber was 4.13×0^{-7} Torr and the gas pressures during deposition were 4 mTorr for Ti and Ni, and 2 mTorr for Cu. These conditions were established from preliminary testing and prior experience in sputtering these materials [2].

For samples with Cu and Ni layer thickness of 25 nm and greater, a total film thickness of 2 μm was deposited. However, for the 10 nm layer thickness a total film thickness of 1.5 μm and greater showed widespread delamination and microcracking, which appeared to be due to higher tensile residual stress. As a result, a 1 μm total film thickness was deposited for the 10 nm layer thickness sample for subsequent residual stress measurement. Bulk monolayers with 500 nm thickness of both Cu and Ni were also deposited using the aforementioned conditions. These were used for initial long-range XRD scans, which were performed primarily to evaluate available peaks for the lattice spacing measurements. Table 1 summarizes details concerning the samples prepared, including the substrate, individual layer and total film thicknesses, as well as the number of layers.

XRD Measurement

A Bruker D8 Discover diffractometer with a LynxEye XE-T detector was used for the 1D XRD measurements. The x-ray source was a copper anode microfocus ($\lambda = 0.154$ nm) with Montel collimating optics. The sample stage was a quarter-circle centric Eulerian cradle equipped with vacuum to hold the samples in place. The samples were positioned using a laser video alignment system. The penetration depths, using 8.04 keV for Cu Kα radiation, were calculated to be ~16 μm at an incident angle of 45°. This is significantly larger than the thickness of any of the films deposited in this experiment. Indeed, when performing the long range scans to facilitate the initial peak selection, the Si (100) peak was seen, confirming penetration through the multilayer to the substrate. Therefore, the stress measured in each of the two layer materials in this study is considered to be the average stress across the whole multilayer film thickness.

To select peaks for stress determination, a 1D XRD scan from 20°-130° 2θ range was performed on the bulk Cu and Ni

Table 1 Sample parameters: number of layers and nominal thicknesses

Thickness			No. of Layers		
Substrate (μm)	Individual layers (nm)	Nominal total film (μm)	Total	Cu	Ni
500	100	2	20	10	10
500	50	2	40	20	20
500	25	2	80	40	40
500	10	1	100	50	50

films. Residual stresses estimated using the XRD method have more consistent results when performed on peaks with 2θ angles greater than 90°, multiple indices, and a relatively high intensity [21]. Based on these guidelines, the Cu (311) and Ni (311) peaks were chosen for residual stress analysis. However, these peaks are also quite close to the Cu (222) peak, which presented a challenge for the peak measurements and stress analysis.

The XRD scans used to capture the Cu (311) and Ni (311) peaks included a 2θ range of 87°-97°, a 2θ step size of 0.1°, and a time per step of 5 s. To improve the signal-to-noise ratio, two additional steps were taken including the use of a 0.6 mm slit and the detector was moved closer to the target to reduce noise from air scatter. Because the sample with 10 nm layers had smaller overall thickness (1 μm) and smaller grain size, a wider 2θ range of 86–101° was used, as well as a longer scan time of 15 s per step to obtain a higher signal-to-noise ratio. Over- and under-travel was utilized on all scans to ensure the completeness of the end regions.

Bruker's EVA software was used to correct for $K\alpha_2$ using a modified Rachinger procedure. The background noise was subtracted out of the scans and a five-point moving average filter was used to smooth the raw data. Over smoothing can cause alternation of the peak shape and position. Therefore, preliminary testing was performed and the 5-point window was confirmed to not alter the peak shape, but effective enough to reduce the noise. A representative 1D scan for the Cu/Ni multilayer sample with 100 nm layers obtained with the aforementioned procedure is shown in Fig. 1.

It is important to highlight the low overall intensity and the overlapping between the adjacent Cu and Ni peaks evident in Fig. 1. Preliminary data acquired using the 2-dimensional (2D) XRD with the XRD^2 method (Pilates 100 K detector & 0.5 mm collimator) and Bruker's LEPTOS software indicated

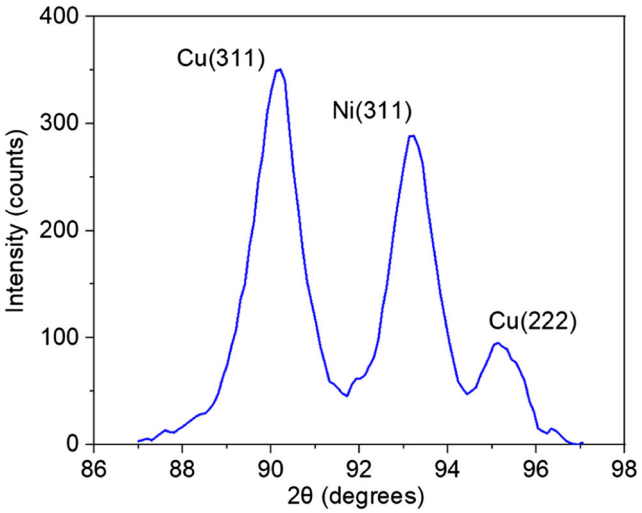

Fig. 1 Representative 1D XRD spectra for the 2 μm thick film sample with 100 nm layer thickness of Cu/Ni. Note the overlap of the Ni and Cu peaks in the saddle regions of the plot

that the in-plane stress was equi-biaxial. Indeed, the equi-biaxial stress is expected due to the rotation of the sample stage during deposition of the metal films. Due to the peak broadening and the low overall peak intensity, the peak position was difficult to determine with confidence because of the inability of the software to determine peak boundaries due to the overlap. As a result, the experimental efforts were then redirected to use 1D XRD measurements and the $\sin^2\psi$ method.

Sin^{2}ψ Method

The $\sin^2\psi$ method uses the shift in XRD peak positions and the out-of-plane tilt angle (ψ) to determine residual stresses via the measured lattice strains and Hooke's law. A schematic diagram defining the directions of the out-of-plane tilt angle (ψ), in-plane tilt (ϕ), and diffraction angle (θ) for measurements of stress in the multilayer Cu/Ni sample surface is shown in Fig. 2. Based on this coordinate system, the strain tensor, $\varepsilon_{\phi\psi}^{\{hkl\}}$ for the equibiaxial stress state is described by [17].

$$\varepsilon_{\phi\psi}^{\{hkl\}} = 2S_1^{\{hkl\}}\sigma_\phi + \frac{1}{2}S_2^{\{hkl\}}\sigma_\phi \sin^2\psi \quad (1)$$

where σ_ϕ is the equi-biaxial residual stress, S_1 and S_2 are constants calculated from the elastic modulus (E), Poisson's ratio (ν), and Hooke's law according to

$$S_1 = \frac{-\nu}{E}, \quad and\ S_2 = \frac{2(1+\nu)}{E} \quad (2)$$

The strain $\varepsilon_{\phi\psi}^{\{hkl\}}$ can be determined from the lattice spacing measurements according to [17].

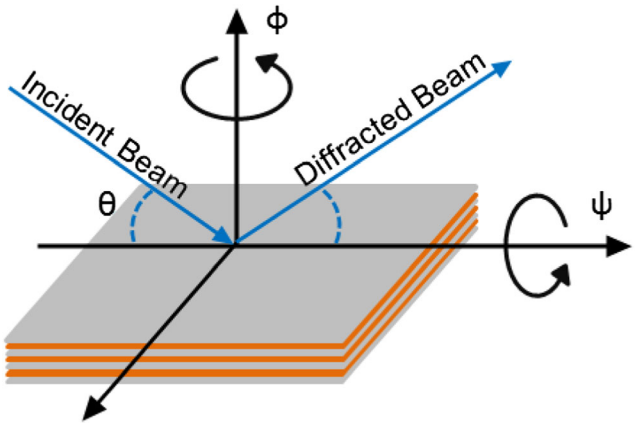

Fig. 2 Schematic diagram showing the diffraction measurement angles ψ, ϕ, and θ in relation to each other and the sample surface after He [18]. The multilayer samples were only tilted in the ψ direction for stress characterization, and not rotated in the ϕ direction due to the equi-biaxial nature of the residual stress

$$\varepsilon_{\phi\psi}^{\{hkl\}} = \frac{d_{\phi\psi} - d_0}{d_0} \tag{3}$$

where $d_{\phi\psi}$ and d_0 are the stressed and stress-free spacing for the {hkl} lattice plane, respectively. Of course, the lattice spacing is determined from Bragg's law and the locations of the diffraction angles of the peaks of interest.

According to published sources [22], the stress-free lattice constants (i.e. d_0 values) for the Cu and Ni were 0.10900 nm and 0.10624 nm, respectively. These constants were confirmed by performing independent XRD measurements of the lattice constants for Cu and Ni powder filings from the Cu and Ni sputtering targets that were annealed in an inert gas environment.

Equation (1) shows that the measured strain $\varepsilon_{\phi\psi}^{\{hkl\}}$ is a linear function of $\sin^2\psi$. The derivative of the simplified strain tensor yields,

$$\frac{\partial \varepsilon_{\phi\psi}^{\{hkl\}}}{\partial(sin^2\psi)} = m = \frac{1}{2} S_2^{\{hkl\}} \sigma_\phi \tag{4}$$

Therefore, the equi-biaxial stress in the multilayer film can be determined directly from the slope m of the strain $\varepsilon_{\phi\psi}^{\{hkl\}}$ distribution plotted as a function of $\sin^2\psi$ [18]. For data collection, five different ψ tilts (0.00, 20.71, 30.00, 37.76, and 45.00°) were selected to give evenly spaced $\sin^2\psi$ values of 0, 0.125, 0.25, 0.375, and 0.5. No ϕ rotations were performed in this work due to the equibiaxial stress state. The strain was plotted against the $\sin^2\psi$ and the residual stress was calculated based on the slope of the linear regression fit of the data.

GMM and EM Algorithm for Peak Position Determination

For low intensity and broad XRD peaks, a determination of peak location is challenging because the maximum value or the middle position half max (MPHM) may be impacted by noise and peak asymmetry. The Center of Gravity (CoG) method calculates the geometric center of the peak and is shown to have the lowest standard deviation in stress in a comparison of five tested methods [20]. The peak location can be determined according to the CoG method from the weighted mean of the intensity distribution described as,

$$\mu = \frac{\sum_{i=1}^{n} w_i x_i}{\sum_{i=1}^{n} w_i} \tag{5}$$

where μ is the weighted mean, w_i represents the intensity (weight) and x_i represents the 2θ angle of each XRD point included. The corresponding weighted variance, σ^2, is calculated by

$$\sigma^2 = \frac{\sum_{i=1}^{n} w_i \left(x_i - \bar{x}\right)^2}{\frac{M-1}{M} \sum_{i=1}^{n} w_i} \tag{6}$$

where M is the number of non-zero intensity points in the distribution and $\bar{x}$ is the weighted mean of the distribution.

The CoG method is sensitive to peak boundary definition, so with overlapping XRD peaks it is critical to deconvolute the peaks before determining the peak position. This was accomplished using two additional algorithms as described below. For a one-dimensional classification of intensity distribution with three overlapping peaks, as shown in Fig. 1, each peak can be treated as a normal or Gaussian distribution and defined as

$$p(x|\mu,\sigma) = P(x_i|G_j) = \frac{1}{\left(\sigma\sqrt{2\pi}\right)} e^{-\frac{(x-\mu)^2}{\sigma^2}} \tag{7}$$

where σ is the standard deviation, σ^2 is the variance, and μ is the mean. This is also called a mixture of Gaussians, or Gaussion Mixture Model (GMM).

When applying the above CoG method, the key is to find the weighted mean (peak position) and variance of the individual distributions. However, since the overlapping intensity contribution to each distribution is unknown, the mean cannot be solved explicitly. The Maximum Likelihood Estimate (MLE) can be used for solving parameters of a distribution with unknown points, and the maximum likelihood of a normal distribution is the mean of the distribution [23]. However, with more than one overlapping distribution where some of the points are unknown, the mean cannot be found using the MLE. Therefore, Bayes Theorem was applied to get a posterior probability equation for each distribution. This posterior probability could be solved if the initial distribution parameters were known, and the distribution parameters could be estimated if the posterior probability was known. The Expectation Maximization (EM) Algorithm is the procedure of holding the distribution parameters constant to calculate the posterior probability, and then recalculating the parameters based on that posterior probability. As these steps in the Expectation Maximization (EM) algorithm are iterated, it can be proven that it will not decrease the log likelihood [24]. Thus for a mixture of Gaussian peaks the MLE for each peak will continue approaching the mean, as long as it does not converge to a local optimum.

To start the EM algorithm, an initial estimate of the mean, standard deviation, and prior point were needed for each probability density function (PDF). The saddle points between the adjacent peaks on the XRD scan were selected as the estimated bounds of the PDFs, and then contributed to these estimates. In this application to the XRD intensity distributions, the "prior" is the total intensity belonging to one distribution divided by the total intensities of all distributions. It is then

recalculated based on the new distribution at each EM iteration.

Once the initial parameters were estimated, the expectation step was performed to calculate the posterior probability for each point in the distributions according to

$$P(G_1|x_i) = \frac{P(x_i|G_1)P(G_1)}{P(x_i|G_1)P(G_1) + P(x_i|G_2)P(G_2) + P(x_i|G_3)P(G_3)} \quad (8)$$

Equation (8) shows the posterior probability of a given point for distribution 1 of 3. $P(x_i|\,G_1)$ is the posterior probability for x_i in the first normal distribution G_1, and $P(G_1)$ is the prior of the first distribution. The posterior probability is calculated for each distribution and then multiplied by the original XRD distribution to get the new intensity distribution. This method includes a soft assignment of the intensity points and is known as the Expectation step. The Maximization step is the recalculation of the weighted mean and variance of each of the PDFs based on the posterior probability. The Expectation and the Maximization steps were iterated 2000 times for each PDF, allowing the peak locations to converge.

Results and Discussion

Multilayer Film Cross Sections and Surface

To confirm the layered structure of the deposited multilayer metal samples, several micrographs were obtained via Scanning Electron Microscopy (SEM) and representative figures are shown in Fig. 3. Cross-section images for the 100 nm and 25 nm layer multilayers are presented in Fig. 3(a) and (b), respectively, and show a clear multilayered structure with alternating Cu and Ni layers. Columnar grains are visible in the Ni layers in Fig. 3(a). This is typical of Ni growth under these sputtering conditions [25]. A grain structure is not clearly visible for the Cu layers due to the ductile fracture surface characteristics and deformation in the Cu layers that occurred when fracturing the samples by flexure. For multilayer samples with 10 nm layer thickness, the 2 μm thick samples delaminated entirely from the Ti layer and Si wafer, while the 1.5 μm thick samples showed uniform microcracking across the whole sample surface as shown in Fig. 3(c). Microcracking was not seen on any of the samples with individual layer thicknesses of 25 nm and greater. Therefore, the visual characteristics suggest that the sample with 10 nm layers possessed a larger tensile residual stress than those of the other layer thicknesses. Since the driving force for film cracking and delamination depends on both the stress amplitude and the film thickness [14], one approach for avoiding the film cracking/delamination is to reduce the total film thickness. Consequently, the 10 nm layer samples were deposited with a 1 μm total stack thickness rather than 2 μm for evaluation of the residual stress. Indeed, these thinner samples showed no signs of microcracking or delamination.

Validation of the GMM and EM Algorithm

There was a concern that the intensity separation and peak positions would depend on the prior that was used for initiation of the EM algorithm. Therefore, preliminary analyses were performed to validate the approach. First, to test the sensitivity of the prior estimates on convergence of the EM algorithm, three pairs of boundary points between peaks were

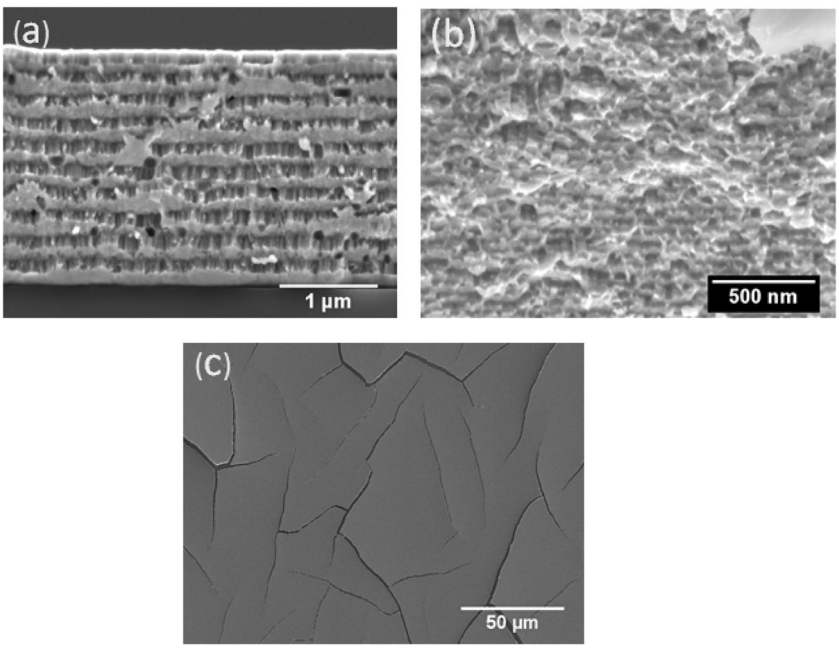

Fig. 3 SEM images of: (**a**) cross-section of the 100 nm layer sample showing alternating layers of Ni and Cu, (**b**) cross-section of the 25 nm layer sample showing alternating layers of Ni and Cu, (**c**) microcracking on the surface of the 1.5 μm thick 10 nm layer sample

evaluated. An example of this effort in application to identify the Cu (311) peak position is shown in Fig. 4. The boundaries are the points that estimate the separation of the intensity distribution (XRD peaks) and example choices of these points are highlighted in Fig. 4(a). The two assigned boundaries and the endpoints divide the XRD scan into three intensity distributions that correspond to the three XRD peaks. The prior is the ratio of the total intensity of one distribution to the total XRD scan intensity. Thus, one prior is generated for each intensity distribution (XRD peak). The "More Accurate" prior assigns the boundaries at the saddle points between the peaks, which are the most intuitive points of separation. The "Less Accurate" and "Inaccurate" priors have boundaries that are chosen further away from the saddle points.

Figure 4(b) and (c) show that the More Accurate and Less Accurate priors resulted in convergence at exactly the same position (90.0917°) for the Cu (311) diffracted peak after sufficient iterations. The More Accurate prior converged to the peak location after ~40 iterations whereas the Less Accurate prior has a less likely estimation of distribution bounds but still converged to 90.0917° after ~60 iterations. The Inaccurate prior is a comparatively poor estimate of the distribution bounds and eventually converged to an incorrect peak position of 88.9157°. Only 80 iterations are shown in the graph for the More Accurate and Less Accurate priors and 450 for the Inaccurate. To maximize the potential for convergence, 2000 iterations were used for each of the diffraction peak analyses that were performed in this investigation. Convergence required a substantially larger number of iterations for the samples with 10 nm layer thickness, but it was achieved successfully within the 2000 iterations.

XRD Scan Profiles

A comparison of the XRD spectra for the five ψ tilts for each multilayer sample is shown in Fig. 5. Specifically, the intensity distributions for the 100 nm, 50 nm, 25 nm and 10 nm multi-layer samples are shown in Fig. 5(a) through (d), respectively. As described previously, the scans were performed on all samples with the exact same scan parameters except for those with 10 nm layers, which were obtained with a tripled scan time, as deemed necessary to increase the signal to noise ratio, and to compensate for the smaller total stack thickness. As layer thickness decreased, all peaks experienced lower intensity and broadening as evident from a comparison of Figs. 5(a) through (c). This resulted in more peak overlap and a decrease in signal-to-noise ratio. In addition, there was clear peak shifting evident to the left for all samples with increasing ψ angle. The shift provides a visual representation of the change in strain with measurement axis, which is key for the $\sin^2\psi$ method. The diffraction peaks exhibited relatively higher intensity as the ψ angle was increased, which could indicate preferred orientation in the samples or an increased x-ray path length due to the penetration angle [17].

With decreasing layer thickness there was a prominent broadening of the Cu (222) peak. In fact, for the 10 nm layer

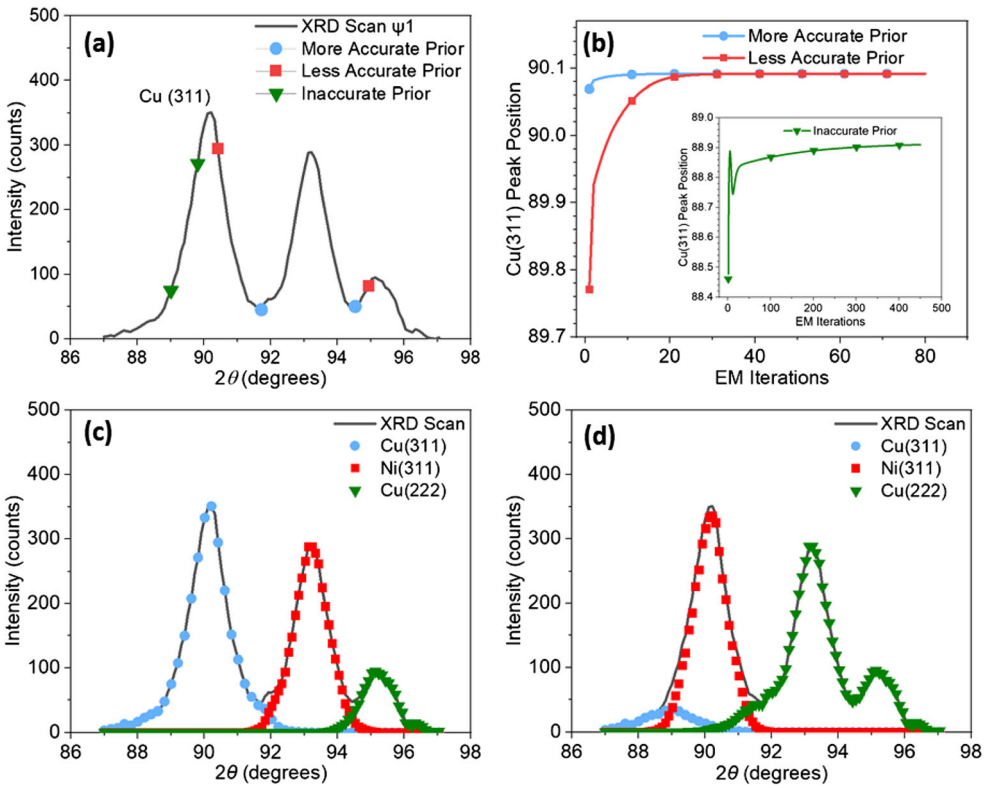

Fig. 4 Determination of the Cu (311) peak position for the ψ1 tilt of the 100 nm sample. Accurate, Less Accurate, and Inaccurate boundaries are used to calculate the means and variances and priors to start the EM algorithm. (**a**) Positions of the 3 pairs of peak boundaries defining priors. (**b**) Convergence of the peak positions based on three different boundaries. (**c**) Deconvoluted peaks based on More Accurate and Less Accurate boundaries. (**d**) Deconvoluted peaks based on the Inaccurate boundaries

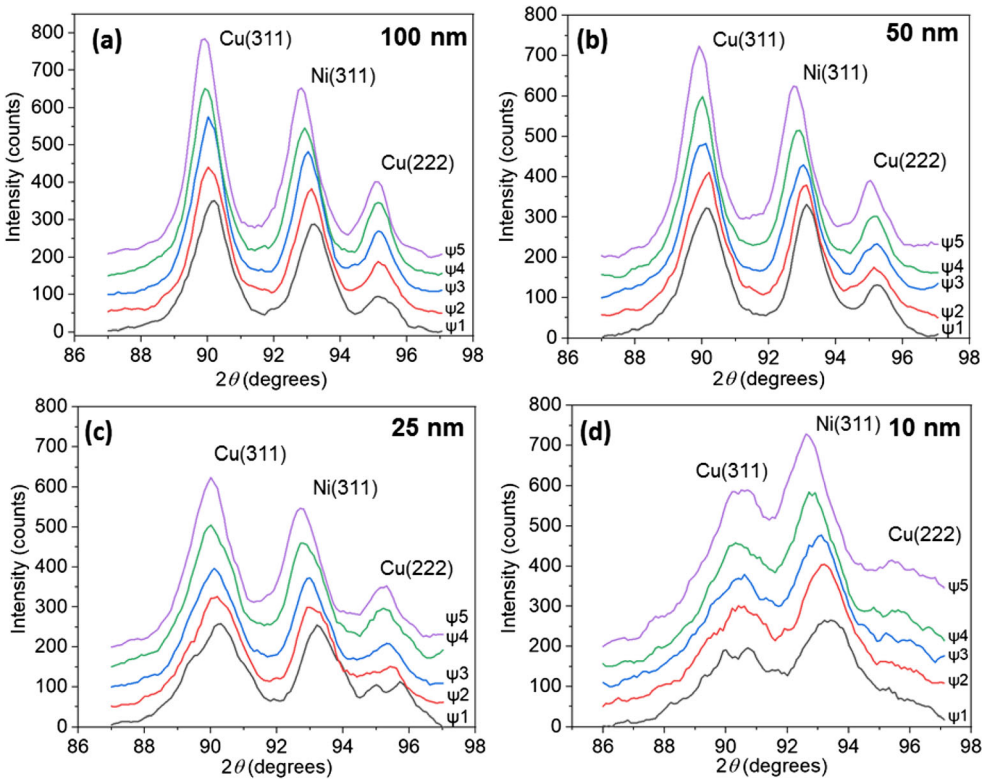

Fig. 5 X-Ray diffraction peak distributions for the (**a**) 100 nm, (**b**) 50 nm, (**c**) 25 nm, and (**d**) 10 nm Cu/Ni multilayer samples at the five different ψ-tilts. Each ψ tilt is offset by 50 counts in the intensity

thickness sample the Cu (222) peak was not necessarily discernable in the diffraction patterns regardless of ψ tilt. Admittedly, this change in diffraction pattern may have contributed to errors in assigning the boundaries of the priors and convergence of the algorithm.

Comparisons of the diffraction peaks over the range in deposited layer thickness after deconvolution are shown in Fig. 6. Specifically, the peak distributions for the Cu (311) and Ni (311) peaks for the ψ1 tilts are shown in Fig. 6(a) and (b), respectively. A comparison of the diffraction peaks in this manner is useful in distinguishing the relative broadening and peak intensity changes with layer thickness for the Cu and Ni separately. Most evident from these figures, the peak intensity decreased, and peak width increased with decreasing layer thickness, especially in the Cu. These changes are most likely due to a decrease in grain size with decreasing layer thickness, which is associated with physical suppression [19]. The direct correlation with layer thickness was not exhibited by the Ni (Fig. 6(b)). For instance, the Ni (311) peak for the ψ1 tilt and 50 nm layer sample has a higher relative intensity when compared to the same peak for the 100 nm layered film. This could suggest a preferred orientation of the grains in the 50 nm sample. The other ψ-tilts for these two samples showed that the 100 nm Ni (311) peaks had consistently higher intensity than the 50 nm layer film, and so on. In addition, the relative intensities of the 10 nm peaks are larger than those for the 25 nm layers due to the longer scan time and its influence on the peak intensity.

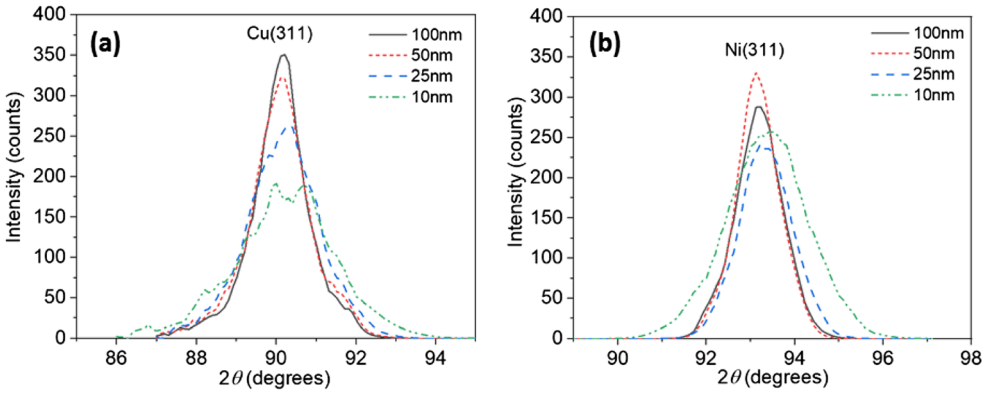

Fig. 6 Comparison of peak profiles post deconvolution by the EM algorithm for the ψ1 tilts at each layer thickness: (**a**) Cu (311) peak, (**b**) Ni (311) peak. Note that the 10 nm peaks are from a film with half the total material thickness as the other peaks, but with a scan that is triple the duration, increasing the overall peak intensity

Strain Vs. Sin$^2\psi$

After the peaks were deconvoluted and the peak positions identified using the COG approach, the strains were calculated according to Eq. (3) for the samples and then plotted as a function of sin$^2\psi$ for each ψ tilt. The equipment used in this experiment is a ¼ circle goniometer, so a calibration test was run to check the alignment and quantify any contribution to the uncertainty of the stress measurements. The annealed Cu powder was scanned at ± ψ tilts using the same angles adopted for evaluation of the film samples. The strain ($\varepsilon_{\phi\psi}$) vs sin$^2\psi$ was plotted to compare results of measurements taken at positive and negative ψ tilts as shown in Fig. 7. Calculation of the residual stress resulted in a difference of 12.7 MPa between the positive and negative ψ tilts for the CoG method; the absolute values in stress for both directions are small, including 45.5 MPa from positive tilts and 31.2 MPa for the negative tilts. This difference is incorporated as part of the uncertainty in the overall measured residual stress of the multilayer samples.

The changes in strain ($\varepsilon_{\phi\psi}$) with sin$^2\psi$ for the multilayer samples are shown in Fig. 8; the responses for the 100 nm, 50 nm, 25 nm and 10 nm samples are shown in Figs. 8a through d, respectively. A linear least squares regression was performed to determine the slope of the strain distribution, which was then used to estimate the residual stress according to Eq. (4). A comparison of the strain ($\varepsilon_{\phi\psi}$) distributions in Fig. 8 show that there are differences in the slopes between the samples. The slope of the Ni layers is higher than that of the Cu for all samples and increases with decreasing layer thickness. The regressions for the Ni also show high degree of linearity in the data and greater R^2 values. In comparison, the slopes for the Cu layers decrease with decreasing layer thickness and is nearly negligible for the 10 nm layer sample.

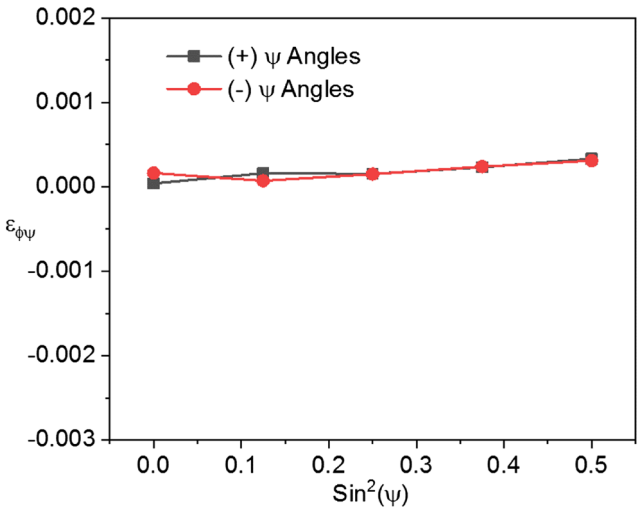

Fig. 7 Calibration measurement of strain ($\varepsilon_{\phi\psi}$) versus sin$^2\psi$ for Cu (311) peaks in the annealed Cu powder. Note the absence of ψ splitting in the responses obtained from positive and negative tilts

While the high degree of linearity suggests an absence of in-plane texture and shear stress [18], a more powerful approach to make this determination is to examine the degree of shear splitting for positive and negative y tilts.

Residual Stress Vs. Layer Thickness

Using the slopes of the strain ($\varepsilon_{\phi\psi}$) distributions with sin$^2\psi$ in Fig. 8, the residual stress in the Cu and Ni layers of each sample was calculated according to Eq. (4). The dependence of the residual stress on layer thickness of the multilayer samples is shown in Fig. 9. The stress distributions show that residual stress in both the Cu and Ni layers are tensile. Furthermore, the residual stress in the Ni layers increases with decreasing layer thickness, which is consistent with the strain distributions in Fig. 8, the largest stress developed in the multilayer sample with the 10 nm layer thickness. The magnitude of stress in the Ni ranges from an average of 880 MPa for the 100 nm layer thickness to 1550 MPa for the 10 nm layer thickness. In general, these results are consistent with the literature as tensile stress are expected in Ni films sputtered in this manner [25]. The residual stress in the Cu layers is also tensile, but substantially smaller and relatively constant at ~250 MPa for layer thicknesses of 25 nm and greater. For the 10 nm sample, the Cu residual stress decreased significantly to just over 20 MPa. The uncertainty in the measured residual stress is shown as error bars in Fig. 9, which includes the standard deviation in the stress estimated for the 100 nm samples along with the error from the goniometer alignment. The 100 nm sample had the most measurements and the largest range and standard deviation. It is possible that the uncertainty is slightly larger than presented here because of the smoothing of the data. However, the trend in residual stress with layer thickness would be unaffected.

Tensile residual stresses are expected for the manner of growth through deposition. The stress in these layers is believed to develop from crystallite coalescence during the growth of each layer [8, 16]. In particular, high tensile stress is observed when grain sizes are small due to crystallite coalescence [8]. Previous work demonstrated that the residual stress in sputtered Cu monolayers is generally tensile and increases with decreasing layer thickness [26]. The Cu residual stresses measured in this experiment fall within the 200 MPa to 400 MPa range reported previously for stress in monolayer films [4, 26], with the exception of the 10 nm sample. One unexpected trend in the data is the constant tensile stress in the Cu layers and then decrease at the lowest layer thickness. One explanation for that behavior is that the stresses in the Ni layers are high enough to invoke yielding in the ductile Cu layers, and a constant residual stress at the ceiling of the flow limit. At the lowest individual layer thickness the stress may cause excessive strain in the Cu, which results in layer failures and stress relief. Admittedly these interpretations are

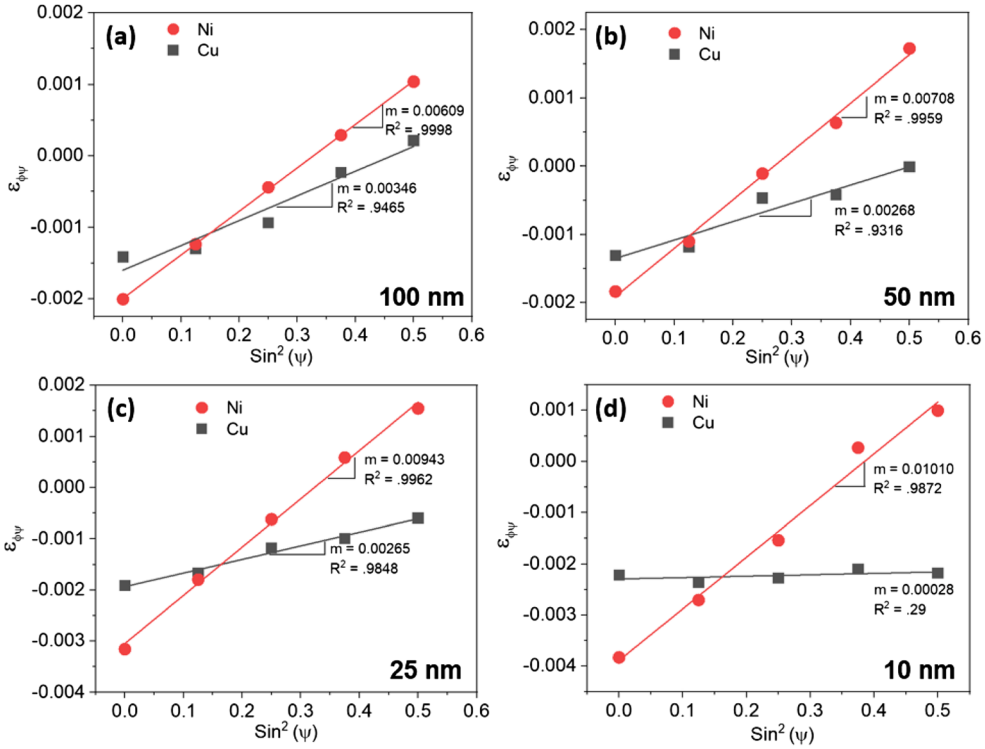

Fig. 8 Measured strain ($\varepsilon_{\phi\psi}$) versus $\sin^2\psi$ of the Ni (311) and Cu (311) peaks for: (**a**) 100 nm, (**b**) 50 nm, (**c**) 25 nm, and (**d**) 10 nm layer samples. Linear least squares regression was used to determine the slopes (m)

speculative and further work is required to understand the cause of the unique trends. Nevertheless, the most important next step in development of multilayer films is to pursue methods for reducing the overall magnitude of the residual stresses.

The layer thickness dependence of the residual stress has wide ranging implications, especially in the development of wear and fatigue resistant coatings. Multilayer thin films of Cu/Ni alternating layers electrodeposited on a polycrystalline electronic grade copper beam increased the fatigue life of samples by more than an order of magnitude [27]. Yet, the residual stresses of the film was not reported. Several possible advantages of the multi-layered structure to the fatigue resistance are cited, such as higher toughness, multilayer interfaces forming slip barriers, and the possible compressive stress in the film [27]. The ability to measure the residual stress in a multilayer thin film with confidence will allow further tailoring of film properties for targeted applications, including fatigue resistance. That is the primary goal of the team's future work.

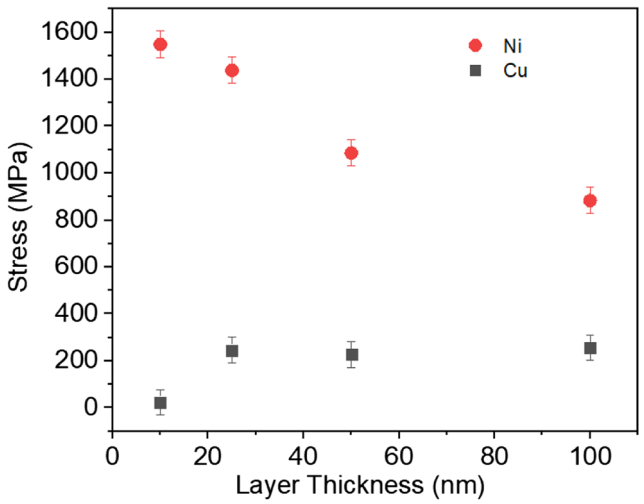

Fig. 9 Residual stress within the Cu and Ni layers for the four multilayer samples plotted as a function of individual layer thickness

Conclusions

In this study, x-ray diffraction and the $\sin^2\psi$ method were adopted to measure the residual stresses in nanoscale metallic multilayer thin films with alternating Cu and Ni layers. The multilayer samples were produced by magnetron sputtering with equal Cu and Ni layer thicknesses ranging from 10 nm to 100 nm. The challenges of peak broadening and peak overlapping in the XRD evaluations, which are caused by the small film and layer thicknesses, as well as small grain size, were addressed by using the Gaussian Mixture Model and Expectation Maximization algorithm in combination with the center of gravity method. Results showed that the residual stress in the multilayer samples was tensile in both the Cu and Ni layers and exhibited a strong layer thickness dependence. The residual stress was substantially higher in the Ni layers than the Cu layers and increased in magnitude with decreasing layer thickness. The measured residual stresses

and trends agreed with results reported for multilayer films prepared under similar deposition conditions measured using the curvature approach. Overall, the results further validate application of the XRD approach with complementary methods for peak identification, and provide improved understanding of the residual stress in nanoscale multilayer thin films. The large tensile residual stresses highlight the importance of seeking unique approaches to mitigate the residual stress in deposited multilayer thin films, particularly for applications involving fatigue.

Acknowledgments The authors acknowledge technical support from the Molecular Analysis Facility (MAF) of the University of Washington for the residual stress analysis. The MAF is a National Nanotechnology Coordinated Infrastructure site at the University of Washington, which is supported in part by the National Science Foundation (grant ECC-1542101), the University of Washington, the Molecular Engineering & Sciences Institute, the Clean Energy Institute, and the National Institutes of Health. Special thanks are extended to Liam Bradshaw for training and consultation on the use of XRD. The team would like to thank Yang Zhou of the UW for his assistance with SEM imaging, as well as Tyler Johnson of the UW for his consultation on classification algorithms.

References

1. Wang J, Zhou Q, Shao S, Misra A (2016) Strength and plasticity of nanolaminated materials. Mater Res Lett 5(1):1–19. https://doi.org/10.1080/21663831.2016.1225321
2. Yang Z, Wang J (2014) Orientation-dependent hardness in as-deposited and low-temperature annealed Ti/Ni multilayer thin films. J Appl Mech 82(1):011008. https://doi.org/10.1115/1.4029058
3. Yang Z, Wang J (2016) Coupled annealing temperature and layer thickness effect on strengthening mechanisms of Ti/Ni multilayer thin films. J Mech Phys Solids 88:72–82. https://doi.org/10.1016/j.jmps.2015.12.005
4. Misra A, HK TEM, Nastasi M (1999) Residual stresses in polycrystalline cu/Cr multilayered thin films. J Mater Res 15(03):756–763. https://doi.org/10.1557/jmr.2000.0109
5. Zheng S, Beyerlein IJ, Carpenter JS, Kang K, Wang J, Han W, Mara NA (2013) High-strength and thermally stable bulk nanolayered composites due to twin-induced interfaces. Nat Commun 4:1696. https://doi.org/10.1038/ncomms2651
6. Misra A, Hoagland RG, Kung H (2004) Thermal stability of self-supported nanolayered cu/Nb films. Philos Mag 84(10):1021–1028. https://doi.org/10.1080/14786430310001659480
7. Khan MI, Bhatti KA, Qindeel R, Althobaiti HS, Alonizan N (2017) Structural, electrical and optical properties of multilayer TiO 2 thin films deposited by sol–gel spin coating. Results Phys 7:1437–1439. https://doi.org/10.1016/j.rinp.2017.03.023
8. Nix WD, Clemens BM (1999) Crystallite coalescence: a mechanism for intrinsic tensile stresses in thin films. J Mater Res 14(08):3467–3473. https://doi.org/10.1557/jmr.1999.0468
9. Chason E, Engwall A, Pei F, Lafouresse M, Bertocci U, Stafford G, Murphy JA, Lenihan C, Buckley DN (2013) Understanding residual stress in electrodeposited cu thin films. J Electrochem Soc 160(12):D3285–D3289. https://doi.org/10.1149/2.048312jes
10. Drory MD, Thouless MD, Evans AG (1988) On the decohesion of residually stressed thin films. Acta Metall 36(8):2019–2028. https://doi.org/10.1016/0001-6160(88)90303-3
11. Czerwinski F, Kedzierski Z (1997) On the mechanism of microcrack formation in nanocrystalline Fe–Ni electrodeposits. J Mater Sci 32(11):2957–2961. https://doi.org/10.1023/a:1018693005002
12. Ghosh SK, Limaye PK, Swain BP, Soni NL, Agrawal RG, Dusane RO, Grover AK (2007) Tribological behaviour and residual stress of electrodeposited Ni/cu multilayer films on stainless steel substrate. Surf Coat Technol 201(8):4609–4618. https://doi.org/10.1016/j.surfcoat.2006.09.314
13. Stoney GG (1909) The tension of metallic films deposited by electrolysis. Royal Society of London A 82:4
14. Freund LB, Suresh S (2004) Thin film materials: stress, defect formation, and surface evolution. Cambridge University Press, Cambridge. https://doi.org/10.1017/CBO9780511754715
15. Abadias G, Chason E, Keckes J, Sebastiani M, Thompson GB, Barthel E, Doll GL, Murray CE, Stoessel CH, Martinu L (2018) Review article: stress in thin films and coatings: current status, challenges, and prospects. J Vac Sci Technol A 36(2):020801. https://doi.org/10.1116/1.5011790
16. Shull AL, Spaepen F (1996) Measurements of stress during vapor deposition of copper and silver thin films and multilayers. J Appl Phys 80(11):6243–6256. https://doi.org/10.1063/1.363701
17. Noyan IC, Cohen JB (1987) Residual stress: measurement by diffraction and interpretation. Springer-Verlag, New York
18. He BB (2009) Two-dimensional X-ray diffraction. John Wiley & Sons, Hoboken, New Jersey
19. He K, Chen N, Wang C, Wei L, Chen J (2018) Method for determining crystal grain size by X-ray diffraction. Cryst Res Technol 53(2). https://doi.org/10.1002/crat.201700157
20. Sedighi M, Nazemnezhad R (2013) Effect of peak positioning method on accuracy of X-ray diffraction residual stress measurement. Exp Tech 40:295–302. https://doi.org/10.1007/s40799-016-0033-9
21. Luo Q, Yang S (2017) Uncertainty of the X-ray diffraction (XRD) sin2 ψ technique in measuring residual stresses of physical vapor deposition (PVD) hard coatings. Coatings 7(8). https://doi.org/10.3390/coatings7080128
22. Swanson HE, Tatge E (1953) Standard X-ray diffraction powder patterns, vol 1. U. S. Dept. of Commerce, National Bureau of Standards, Washington
23. Duda RO, Hart PE, Stork DG (2012) Pattern classification. John Wiley & Sons, Hoboken
24. Bousquet O, von Luxburg U, Rätsch G (2011) Advanced lectures on machine learning: ML summer schools 2003, Canberra, Australia, February 2–14, 2003, Tübingen, Germany, august 4–16, 2003, revised lectures, vol 3176. Springer-Verlag Berlin, Heidelberg
25. Mitra R, Hoffman RA, Madan A, Weertman JR (2011) Effect of process variables on the structure, residual stress, and hardness of sputtered nanocrystalline nickel films. J Mater Res 16(04):1010–1027. https://doi.org/10.1557/jmr.2001.0142
26. Zhang X, Misra A (2004) Residual stresses in sputter-deposited copper/330 stainless steel multilayers. J Appl Phys 96(12):7173–7178. https://doi.org/10.1063/1.1813617
27. Stoudt MR, Ricker RE, Cammarata RC (2001) The influence of multilayered metallic caoting on fatigue crack nucleation. Int J Fatigue 23:S125–S223